Cement and Concrete Research 134 (2020) 106088

Contents lists available at ScienceDirect

Cement and Concrete Research

journal homepage: www.elsevier.com/locate/cemconres

Influencing factors on micromechanical properties of calcium (alumino) silicate hydrate C-(A-)S-H under nanoindentation experiment

Rotana Hay[a], Jiaqi Li[b], Kemal Celik[a,*]

[a] Division of Engineering, New York University Abu Dhabi, P.O. Box 129188, Abu Dhabi, United Arab Emirates
[b] Department of Civil and Environmental Engineering, University of California at Berkeley, 94720 Berkeley, United States

ARTICLE INFO

Keywords:
Nanoindentation
Calcium (alumino) silicate hydrate
Micromechanical properties

ABSTRACT

In Portland cement-based concrete, calcium (alumino) silicate hydrate (C-(A-)S-H) is the principal binding phase that governs its physical, mechanical, and durability properties. In this study, micromechanical properties of compacts made of synthetic C-(A-)S-H powder were investigated with nanoindentation, and various influencing factors were identified. It was revealed that a normal distribution and convergence of test data could be attained with an indentation depth > 350 nm. Higher conditioning relative humidity, pressure, and holding time aided consolidation of the powder and led to an improved elastic modulus. No remarkable influence of strain rate (0.025–0.1 s^{-1}) and vibration frequency was noted. While the Al-incorporated C-A-S-H exhibited superior mechanical properties relative to C-S-H, all the C-(A-)S-H compacts yielded lower elastic modulus values as compared to data from fully hydrated C_3S paste, mainly attributable the phase bonding, packing density, chemical composition, and the presence of phases other than C-(A-)S-H in the C_3S sample.

1. Introduction

The hydration of the ordinary Portland cement (OPC) produces calcium (alumino) silicate hydrate C-(A-)S-H [1–3], which serves as the principal binding phase of our modern OPC-based concrete. Significant uptake of aluminum (Al) into the hydration product is prevalent when the OPC is partially replaced with supplementary cementitious materials (SCMs) of high alumina (Al_2O_3) content [4,5]. Al-incorporated C-S-H is termed C-A-S-H [6]. In this text, C-(A-)S-H (A in brackets) is also used to annotate general hydration products of these two possible forms. C-(A-)S-H governs the physical and mechanical properties of Portland cement-based concrete [7]. Understanding the micromechanical behavior of C-(A-)S-H is thus essential to unraveling the fundamental physics and improving the engineering performance of the construction materials. Nanoindentation is one of the direct techniques used to measure the mechanical properties of materials at a submicron scale and has been applied on solid, soft polymers, or even biomaterials [8–12]. The technique has also been widely adopted for micromechanical characterization of cement-based materials. An early work on pure constituents of Portland cement clinker showed that C_3S, C_2S, C_3A, and C_4AF exhibited a similar range of elastic moduli between 125 and 145 GPa [13]. Hydrated cement pastes, on the other hand, exhibited a bi-modal property dominated with low-density (LD) and high-density (HD) C-(A-)S-H phases with mean elastic modulus values of 21.7 GPa and 29.4 GPa, respectively, independent of water-to-binder ratios [14,15]. The LD and HD C-(A-)S-H were associated with hydrates within capillary space (outer products) and confined regions (inner products), respectively. The notion of LD and HD forms of C-(A-)S-H in hydrated cement matrix has been widely embraced by the cement research community. In quantifying the micromechanical properties of these two forms of C-(A-)S-H and other phases in hydrated cement samples, statistical nanoindentation in which a large number of single indentations are performed in a grid, and followed by deconvolution and peak assignment using statistical methods have been widely adopted. A corresponding wide range of elastic modulus data have been reported to be 16.8–25.2 GPa [16,17] for LD C-S-H and 29.1–41.5 GPa for HD C-S-H [18,19]. A summary of such data could be found in [20–22].

Using a virtual experiment with nanotomography verification, other researchers demonstrated that homogeneous phase-pure C-S-H regions in hydrated cement pastes are too small to induce independent distributions in elastic modulus frequency plots, raising questions on the application of statistical nanoindentation for mechanical characterization of pure phases in hydrated cement pastes [23,24]. Impurities inherent in C-(A-)S-H phases such as nano-crystalline $Ca(OH)_2$ were found to significantly increase its elastic modulus [25]. Various other factors have also been shown to influence indentation results of cement-based materials: surface roughness [26], indentation load intensity and

* Corresponding author.
E-mail address: kemal.celik@nyu.edu (K. Celik).

https://doi.org/10.1016/j.cemconres.2020.106088
Received 24 August 2019; Received in revised form 19 April 2020; Accepted 20 April 2020
Available online 13 May 2020
0008-8846/

the associated microcracks [27], presence of foreign ions (e.g., Al) [28], and Ca leaching or Ca/Si molar ratios within C-(A-)S-H formulations [14,27,29]. A coupling of nanoindentation and scanning electron microscopy equipped with energy dispersive spectroscopy (SEM-EDS) was introduced to correlate the micromechanical properties to phases in cement pastes based on their chemical information [25,30,31]. The technique was implemented with a multivariate mixture modeling by following hardness, elastic modulus, and intensities of silicon, calcium, and aluminum to yield phase clustering and its associated micromechanical properties [32]. Quantitative EDS was incorporated to better reveal the chemical and micromechanical signatures of phases in cement pastes [21,33]. Nevertheless, the technique also comes with its inherent limitations, including matching of micro-volumes sensed by both the nanoindentation and EDS techniques, scale separability for intrinsic phase representation [31], and signal and strain energy gradient under the indenter [34]. Yet, the technique confirmed a rare occurrence of pure C-S-H in cement paste system, and an intermix of phases or inclusion of submicron impurities (calcium, aluminum, sulfur, and anhydrous materials) into the outer region of C-S-H was found to be prevalent [21,32].

To circumvent these challenges, evaluation of micromechanical properties of C-(A-)S-H using nanoindentation could be performed with a compressed form of pure C-(A-)S-H powder [20]. The use of compressed C-(A-)S-H powder, subsequently termed compact in this text, has attracted significant attention as single-phase C-(A-)S-H with variable compositions or intermixes with polymers can be readily synthesized without considering the heterogeneity inherent in hardened cement pastes [35]. While the intensity of the maximum applied load during indentation exhibited a negligible effect on the micromechanical properties of compressed C-(A-)S-H [27], a positive correlation between elastic modulus and compact density was observed [36]. A number of other parameters, including moisture content, silicate polymerization, and Ca/Si ratio in C-(A-)S-H composition, have been speculated to contribute to the difference in mechanical responses of C-(A-)S-H compacts [29]. Also, it is yet unclear if compressed C-(A-)S-H could be used to represent the properties of the true phase in cement pastes or concrete after all. A considerable deviation in elastic modulus values between C-(A-)S-H in hardened cement pastes and those in compacts has been reported, with compressed synthetic C-(A-)S-H generally displaying lower mechanical properties [20].

A comprehensive study is hence needed to elucidate the influence of different factors on micromechanical properties of the compressed form of pure C-(A-)S-H powder. This paper aims to investigate the effects of conditioning environment, holding time of the pressure implemented in compact preparation, pressure level, and indentation test parameters on the elastic modulus of compressed C-(A-)S-H powder using the nanoindentation technique. For comparison, a mature tricalcium silicate (C_3S) paste was also used in the indentation experiment. Thermal gravimetric analysis (TGA) and Raman spectroscopy were also used to comprehend the chemical composition of the materials used. The outcome of the present study could serve as a guideline to obtain more reliable and reproducible results for elastic modulus or hardness data from the nanoindentation of compressed C-(A-)S-H powder. It would help to improve the significance of this technique to unravel the micromechanical properties of the phases in hydrated cement pastes.

2. Materials and methods

2.1. Materials

C-(A-)S-H samples were synthesized with a constant bulk Ca/(Al + Si) molar ratio of 1, while bulk Al/(Al + Si) molar ratios were fixed at 0 (A0 or C-S-H) and 0.1 (A1 or C-A-S-H). The samples were cured at 80 °C in Teflon bottles for three months by mixing stoichiometric contents of SiO_2 (Aerosil 200, Evonik), CaO, and/or $CaO{\cdot}Al_2O_3$ powder at a water-to-solid mass ratio of 45 in an N_2-filled glove box. The relatively high temperature was adopted in order to achieve a quick equilibrium of a phase-pure product at about 56 days [37] and to mimic the internal condition of typical mass, geopolymer, and precast concrete, which usually experiences high internal temperature induced by either heat of hydration or high-temperature curing. The solid C-(A-)S-H samples were extracted by vacuum filtering using 0.45 μm nylon filters and then drying in N_2-filled desiccators in the presence of NaOH pellets for 14 days, followed by freeze-drying for 4 days. C_3S paste (designated as C3S) with a water-to-binder ratio of 0.5 was also used for indentation comparison. The paste was cured in a closed container (flushed with nitrogen gas before sealing) for 90 days before vacuum sealing for another 210 days. At 300 days, isopropanol was used to stop the hydration of the C_3S sample which was then vacuum dried for another 3 days before further analyses.

2.2. Thermogravimetric analysis

The powder C-(A-)S-H and ground hydrated C_3S samples were used for thermo-gravimetry/differential thermal analysis with SQ600 TG/DTA series. Approximately 20 mg of each sample was manually compacted into an alumina crucible and immediately transferred to the analyzer chamber. The temperature was regulated from 25 °C to 1000 °C with a constant ramping rate of 10 °C/min under N_2 gas at a flow rate of 100 ml/min.

2.3. Sample conditioning and compact preparation

The C-(A-)S-H samples were subsequently conditioned until stable weights were achieved under three environments: (i) as received from freeze-drying in sealed containers at room temperature, (ii) room temperature (22–24 °C) under 11% relative humidity (RH) using saturated lithium chloride (LiCl) with the procedure as outlined by other researchers [1,29,36], and (iii) room temperature under 75% RH using saturated sodium chloride (NaCl) [38]. In the compact making process for nanoindentation, two parameters focusing on pressure level and holding time were investigated. The pressure intensity would create different porosity levels, which would exert an influence on the micromechanical properties of C-(A-)S-H. Similarly, the holding time was postulated to induce compaction and creep within the matrix and hence would also affect the mechanical response of the resulting C-(A-)S-H compacts. Other parameters of interest include loading/unloading frequency and strain rates implemented in the nanoindentation test set-up.

0.1 g of the conditioned samples were retrieved from the conditioning environments, and manually compacted into the sample compartment of a 5 mm-diameter die lubricated with a thin layer of PTFE heavy-duty lubricant to reduce skin friction and to improve load transfer efficiency. Two end disks polished to mirror finish were used to sandwich the powder to yield compacts with a roughness fit for direct nanoindentation. The sample compression and unloading were done with a 100 kN-capacity Universal Testing Machine (UTM) at a loading rate of 0.5 mm/min to a different target or apparent pressures.

2.4. Raman spectroscopy

Raman spectra for all samples prepared under different conditioning environments and pressures were recorded with a confocal Raman microscope (alpha300 RA from WITec GmbH, Ulm, Germany) under 488 nm laser source. The detector used was an SP2300i from Princeton Instruments (Acton, MA) equipped with a triple grating turret and Peltier cooled at −60 °C. An 1800 lines/mm grate was selected for high resolution scanning from 100 cm^{-1} to 1200 cm^{-1}. Calibration was performed on a silicon wafer using the 520 cm^{-1} emission band. The objective used was a Zeiss EC Epiplan 20× with a working distance of 3.2 mm. At the start, an optical microscope image of the sample was recorded, and after focusing, the laser position was aligned. Point data acquisition in Confocal Raman mode was performed with an integration

time of 5 s and averaged over 10 scans. Data analyses were performed with Project 5.0 software from Witec. First wave numbers of the spectra were recalibrated to achieve the Rayleigh band to value as close as possible to zero by modifying the excitation wavelength. Then, Raman signal analysis was initiated with the following steps: (i) Cosmic Ray Removal, (ii) data smoothing with Savitzky-Golay function, and (iii) background subtraction with a shape size between 30 and 60.

2.5. Nanoindentation

The C-(A-)S-H compacts were mounted on an aluminum platform using a thermoplastic adhesive polymer to fix them in place. After drying, the C_3S sample was embedded in high-viscosity epoxy. The assembly was ground with sandpaper to remove the epoxy layer and to expose the sample surface prior to sequential polishing with oil-suspended diamond particles of size ranging from 9, 6, 1 to 0.05 μm.

Grid nanoindentation was then performed on the sample surfaces with Keysight G-200 Nanoindenter using a diamond Berkovich tip. For comparative analysis, two indentation techniques called Basic and Continuous Stiffness (CSM) methods were adopted to measure the elastic modulus of the synthetic C-(A-)S-H samples. In the Basic method, the hardness and modulus properties of the material are measured at a target indentation depth [14,39]. For this study, the main target indentation depth of 350 nm with a peak load hold time of 10 s to account for creep and thermal drift was implemented. This target indentation depth of 350 nm was used to achieve optimum interaction volume larger than the nanogranular globules [18] but smaller than the homogeneous isotropic region of a typical phase [23]. On the other hand, the CSM method induced a sinusoidal load at a selected frequency during the loading branch and thus allowed for continuous measurement of the elastic modulus throughout the indentation depth, which was set to a target of 2000 mm. Both the Basic and CSM methods are graphically illustrated in Fig. 1. One useful application of the CSM method is to investigate the uniformity of the phases within the samples throughout the indentation depth or the effects of substrate on the mechanical properties of thin films [40,41]. A surface detection limit was set to 200 N/m for both the methods, and a total of 72 indentation points were performed on each C-(A-)S-H sample while a total of 225 points were conducted on the C_3S sample due to phase heterogeneity. A grid spacing of 50 μm was implemented. A Poisson's ratio of 0.24 as adopted by other researchers for C-(A-)S-H was applied in the stiffness calculation [15]. Fused silica was also used as a reference and tip calibration. As both elastic and plastic deformations concurrently occurred during indentation loading, only the initial unloading portions of the load-displacement curves are used in the elastic modulus calculation [42].

The hardness (H) and effective indentation modulus (E_r), which takes into account deformation of the indenter during loading, can be found from Eqs. (1) and (2), respectively [13].

$$H = P/A \tag{1}$$

$$E_r = S\sqrt{\pi}/(2\beta\sqrt{A}) \tag{2}$$

where P is the load applied to the test surface, A is the projected contact area which is a function of indentation depth upon surface contact, S is the contact stiffness derived from the initial portion of the unloading curve, and β is the correction factor for indenter geometry (1.034 for Berkovich tip [39]). The elastic modulus of the material (E_p) is obtained using Eq. (3):

$$1/E_r = (1 - \upsilon^2)/E_p + (1 - \upsilon_i^2)/E_i \tag{3}$$

where υ is the Poisson's ratio for the test material, E_i and υ_i are the elastic modulus and Poisson's ratio, respectively, of the indenter. For a diamond tip, $E_i = 1141$ GPa and $\upsilon_i = 0.07$ [39].

Table 1 summarizes the parameters and corresponding sample annotations, in which RH stands for the relative humidity, VA for humidity of as-received condition (freeze-drying), P for the applied pressure implemented in making the compact, T for the holding time, S for the strain rate and F for the frequency. Numerical values of 0, 1, 2, and 3 were assigned for pressure levels of 50, 95, 200, and 300 MPa, respectively. A similar numerical assignment was used for the strain rate and frequency. For test setup parameters, both loading or strain rates and frequency were investigated. Hence, a typical sample annotation A0-RH11-P1-F1-S2 refers to A0 conditioned at 11% RH (RH11) with the compact prepared at 95 MPa (P1), tested under a frequency of 45 Hz (F1) and a strain rate of 0.01 S^{-1} (S2).

2.6. Nitrogen (N_2) gas adsorption

N_2 gas adsorption was performed with a 3Flex surface analyzer (Micromeritics, USA) on selected compacts to investigate their porosity properties. The samples were degassed under a pressure of 0.1 mmHg and at a temperature of 40 °C for 24 h [43,44] to preserve the composition and to remove surface moisture and organic contaminants. The adsorption and desorption characteristics were conducted at −196 °C, the liquid temperature of N_2, and with applied pressure (P) varied between 1.3×10^{-9} and 1 with respect to the saturation pressure of N_2 (P_o). Specific surface area (SSA) was derived from the linear region of the adsorption-desorption curves.

2.7. Scanning electron microscopy (SEM)

SEM of selected pressed samples was conducted with Quanta FEG 450 under the backscattered electron (BSE) mode to observe the surface roughness and indented regions of selected C-(A-)S-H compacts. No coating was applied to prevent the possible filling of the indented areas and the porosity. The images were captured at 3 kV with a probe current of 2.5 nA.

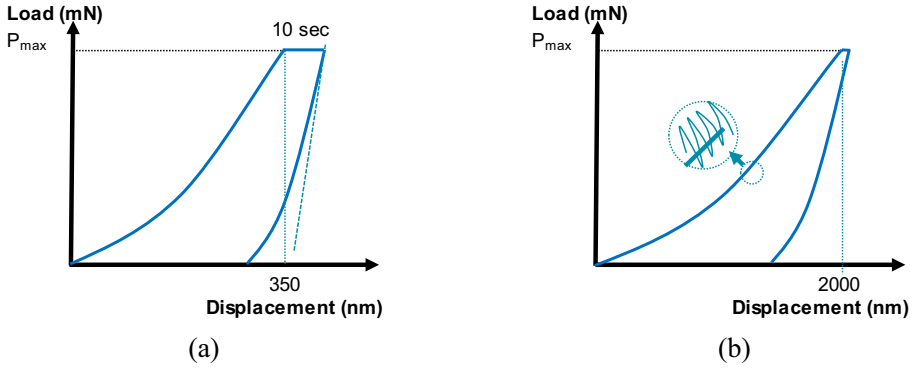

Fig. 1. Graphical illustration of: (a) Basic, and (b) CSM method.

Table 1
Conditioning, pressing, and nanoindentation test parameters.

Sample	Conditioning			Pressing		Test parameters		Annotation
	Vacuum	11% RH	75% RH	Pressure (MPa)	Holding time (min)	Frequency (Hz)	Strain rate (s^{-1})	
A0	✓			95	30	–	–	A0-VA-P1-T30[a]
		✓		95	30	–	–	A0-RH11-P1-T30[a]
			✓	95	30	–	–	A0-RH75-P1-T30[a]
A1	✓			95	30	–	–	A1-VA-P1-T30[a]
		✓		95	30	–	–	A1-RH11-P1-T30[a]
			✓	95	30	–	–	A1-RH75-P1-T30[a]
A0		✓		95	0	–	–	A0-RH11-P1-T0[a]
		✓		95	60	–	–	A0-RH11-P1-T60[a]
A0		✓		50	30	–	–	A0-RH11-P0-T30[a]
		✓		200	30	–	–	A0-RH11-P2-T30[a]
		✓		300	30	–	–	A0-RH11-P3-T30[a]
A0		✓		95	30	–	0.025	A0-RH11-P1-S0[b]
		✓		95	30	–	0.1	A0-RH11-P1-S2[b]
		✓		95	30	22.5	0.05	A0-RH11-P1-F0[c]
		✓		95	30	45	0.05	A0-RH11-P1-F1[c]
		✓		95	30	60	0.05	A0-RH11-P1-F2[c]
		✓		95	30	45	0.025	A0-RH11-P1-F1-S0[c]
		✓		95	30	45	0.05	A0-RH11-P1-F1-S1[c]
		✓		95	30	45	0.1	A0-RH11-P1-F1-S2[c]

[a] Tested under both the Basic method with a strain rate of 0.05 s^{-1} and the CSM method with a frequency of 45 Hz and a strain rate of 0.05 s^{-1}.
[b] Tested under the Basic method only.
[c] Tested under the CSM method only.

3. Results

3.1. Powder compression and unloading

Typical compression responses of the C-S-H powder sample loaded to different target pressures in the pressing die are depicted by conventional stress-displacement curves and Heckel plots in Fig. 2(a) and (b), respectively. The Heckel representation correlates the relative density of the compact to the applied pressure and is based on Eq. (4) [45] where D is the relative density (density ratio), P is the applied pressure, and K and C are constants. The equation was derived based on an analogy to a first-order chemical reaction with porosity being the reactant and density being the product. D was estimated by dividing the apparent density of a compact at pressure P by the particle density. The apparent density could be calculated by taking the ratio between the sample mass and the compact volume at the respective pressure level. In the case of C-(A-)S-H, a wide range of particle or globule density has been reported to vary from 2.03 to 2.85 g/cm^3, depending on the moisture state in the solid structure, surface moisture, and inter-particle water [46,47]. Under 11% RH, the density of C-(A-)S-H has been reported to be 2.47 g/cm^3 [47,48], and this value was adopted in this study.

$$\ln\left(\frac{1}{1-D}\right) = kP + C \tag{4}$$

It is observed in Fig. 2(a) that the stress-displacement responses of the three samples exhibited a similar trend, although the curves did not overlap, attributable to different levels of initial compaction as done manually. As the stress increased, the slopes of the curves also increased as a result of sample densification, implying an increase in stress with strain at an increasing rate, as also observed by other researchers [49]. Subsequently, squashing of particles, and a reduction in inter- and intraparticulate voids and bonding occurred, and a cohesive mass was formed [50]. Toward the end of the compression, holding the loading platen when the target load was achieved led to a decrease in the resulting stress, attributed to particle rearrangement and further consolidation. Highlighted by a dotted circle in Fig. 2(a) is a sudden small jolt in the stress-displacement curve in A0-RH11-P3-T30 due to a slight misalignment between the plunger and the mouth of the sample compartment of the die. The plots in Fig. 2(b) revealed that the Heckel profiles could be classified into two main regions: (i) low-pressure (< 25 MPa) curvature arising from slippage and rearrangement of particles [51], and (ii) linearity caused by plastic deformation of particles under pressure [52]. In the latter region, the responses followed an almost linear relationship and confirmed the compressibility of C-(A-)S-H in accordance with Eq. (4). It is expected that the Heckel plots normalized to the natural logarithm of porosity would give the same stress-displacement responses (profiles and slopes) at all target pressure levels. This is not the case, and the slight deviation could be attributed to different levels of initial manual compaction and friction between the die body, the sample and the polished steel pellets used to sandwich the sample powder.

3.2. Characterization

3.2.1. Thermogravimetric results

Weight loss and differential weight loss results for the C-(A-)S-H and C_3S paste samples are given in Fig. 3. Early mass losses with endothermic peaks of centers between 80 and 145 °C corresponded to dehydration or mass loss of interlayer and structurally bound water in the C-(A-)S-H system [37,53]. Higher humidity led to higher adsorption of water into C-(A)-S-H structure and thus resulted in a more prominent endothermic peak in the vicinity of 50 °C for A0-RH75 and A1-RH75. This early dehydration peak could be attributed to the drying of condensed water from the gel nanopores between C-(A-)S-H globules [47,54,55] and partly to the loss of the interlayer water through instantaneous migration from interlayer spaces to larger gel pores [56]. Similar relative sample weight and differential weight loss profiles up to 200 °C for both A0 and A1 under freeze-drying and 11% RH indicated a similar moisture adsorption characteristics and level of the two samples. It is known that dehydroxylation of $Ca(OH)_2$ exhibits an endothermic peak at around 460 °C while decarbonation of $CaCO_3$ takes place from 600 °C to 800 °C [57]. The current results showed there were no apparent narrow peaks at 460 °C for all C-(A-)S-H samples, indicating that there was a negligible content of $Ca(OH)_2$ in the samples. The absence of $Ca(OH)_2$ in both A0 and A1 was also confirmed by X-ray diffraction (XRD) analysis results, which are given in Fig. A.1 of Appendix A as Supplementary information. The broad peak in the vicinity of 500 °C in the two C-(A-)S-H sample groups was hence attributed to the decomposition of C-(A-)S-H [37]. In contrast, a prominent

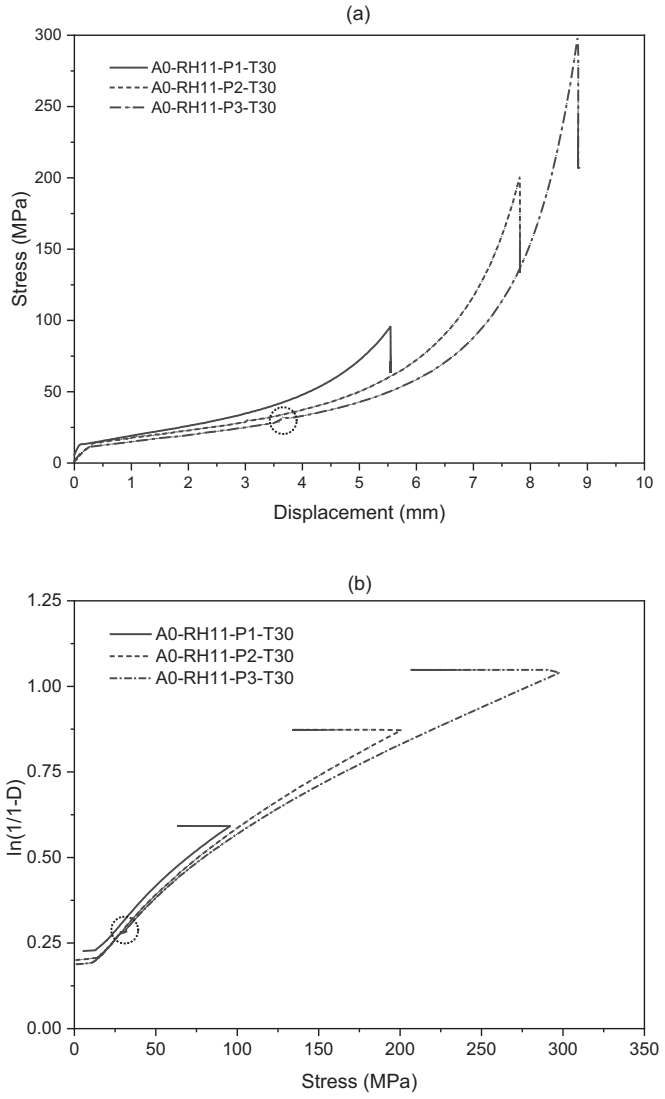

Fig. 2. Stress responses for C-S-H (A0) under 11% RH (RH11) loaded to different target pressures of 95 (P1), 200 (P2), and 300 MPa (P3): (a) stress-displacement curves, and (b) Heckel plots.

endothermic peak at 460 °C in C_3S confirmed a prevalent presence of Ca $(OH)_2$ as one of the main hydration products in the sample. Using the tangential method between 400 and 500 °C [57], the content of Ca $(OH)_2$ was estimated to be 24.4% in the C_3S sample at 300 days. The weak endothermic peaks between 600 and 800 °C in C-(A-)S-H samples conditioned under a relative humidity of 75% implied their slight carbonation which may have occurred during the sample handling. Negligible carbonation was also observed in C3S, as reflected by a weak endothermic peak at 625 °C. The decomposition of C-(A-)S-H to wollastonite ($CaSiO_3$) [58] occurred in all the C-(A-)S-H samples, as reflected by a prominent peak in the vicinity of 810 °C. An absence of the endothermic peak at 810 °C for C3S implies that more stable C-(A-)S-H products were formed in the system. It is also interesting to note that as compared to A0-RH75, A1-RH75 showed an ultimate mass loss level similar to samples conditioned at lower humidity levels and could be attributed to the enhanced cross-linking of C-(A-)S-H products with the presence of Al [37] and the resulting ability to accommodate less of the structurally bound water in the system.

3.2.2. Raman spectroscopy results

Fig. 4 presents Raman spectra obtained for external surfaces of C-(A-)S-H compacts. All bands below 400 cm^{-1} are probably due to Ca–O

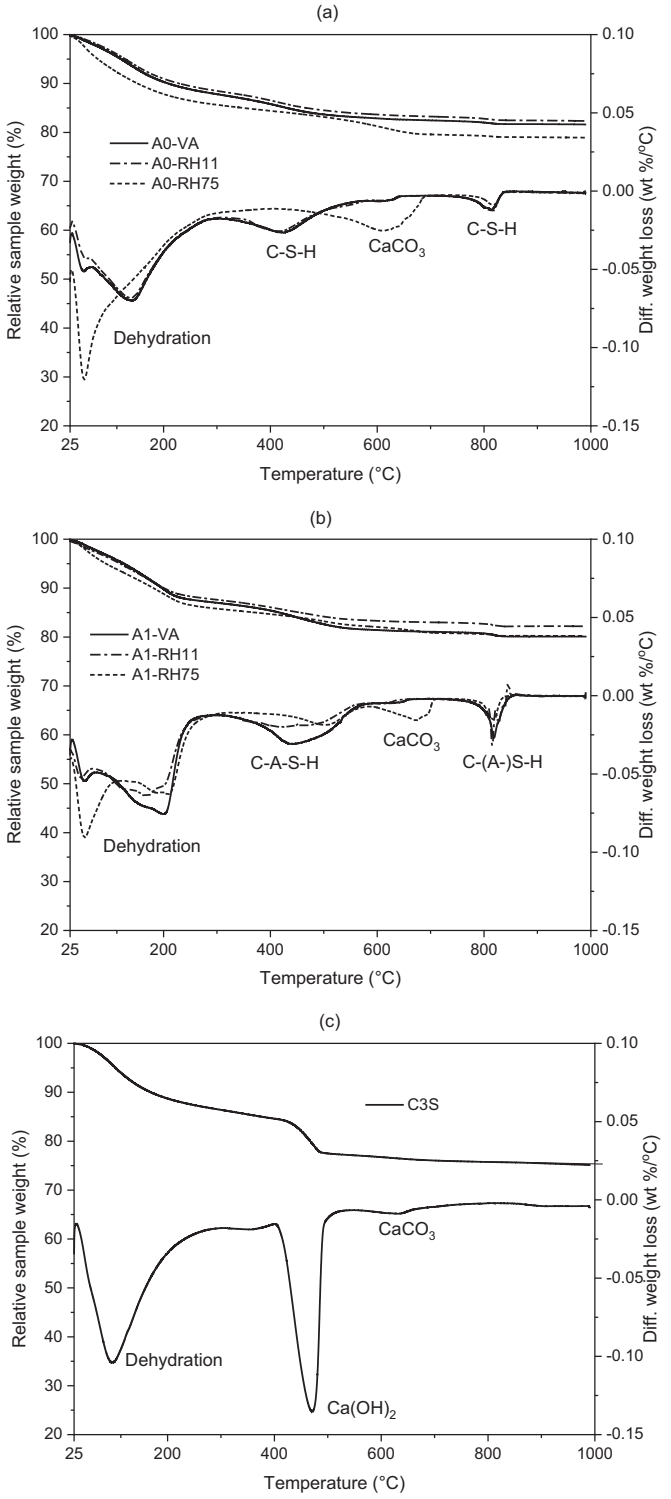

Fig. 3. Thermal gravimetric analysis results for: (a) C-S-H (A0), (b) C-A-S-H (A1) under as-received condition (VA), 11% RH (RH11), and 75% RH (RH75), and (c) C_3S paste at 300 days.

vibration [59]. Specifically, the broad peak in the 305.4 cm^{-1} region was attributed to the lattice vibration of Ca–O polyhedral [60]. Ca $(OH)_2$ was shown to have a spectrum at 356 cm^{-1} [61], and its absence confirms that $Ca(OH)_2$ was not present in the system, consistent with the TGA results. The peak at 444.1 cm^{-1} was attributed to non-bridging oxygen atoms of SiO_4 [62]. The peak at 600–700 cm^{-1} was due to the symmetric stretching motion or vibration of the Si-O-Si bridges, while

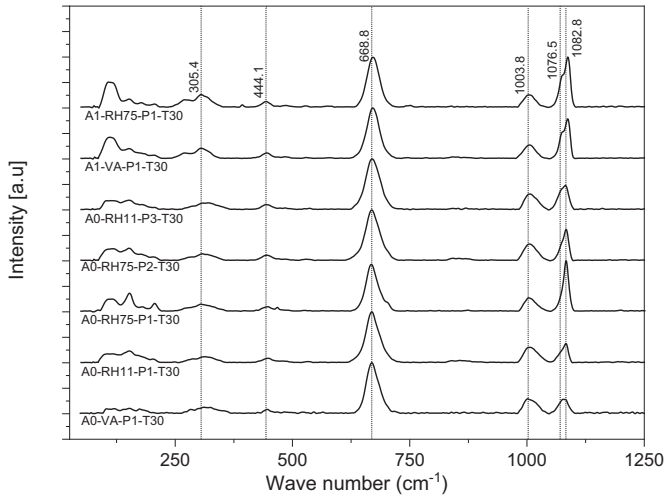

Fig. 4. Raman spectroscopy of C-S-H (A0) and selected C-A-S-H (A1) under as-received condition (VA), 11% RH (RH11), and 75% RH (RH75).

the peak in the 1000 cm^{-1} region was a result of Si–O stretching range at Q^2 sites [59,63]. Si–O vibration at Q^3 sites contributed to a weak shoulder appearance at 1040 cm^{-1} or higher in the presence of Al [62]. On the other hand, the C–O spectrum with peaks at 1082.8 cm^{-1} [59,62] were observed to be present in all samples, attributable to possible surface carbonation and formation of $CaCO_3$ polymorphs. The carbonation could predominantly occur after the indentation as the samples were to some extent exposed to air before the Raman spectroscopy. It is important to note that the Q^1 peaks at 883–955 cm^{-1} were not intense, suggesting a long-range order of the (alumino) silicate chains of C-(A-)S-H synthesized at 80 °C, which is consistent with a study conducted by Ortaboy et al. [62].

3.3. Nanoindentation results from Basic method

3.3.1. Load-indentation depth response

The load-indentation depth response for all the 72 indentation points of A0-RH11-P1-T30 is graphically presented in Fig. 5. A linear-plastic response was observed during the loading stage, after which the 10 s holding time led to deformation at a constant peak load beyond the 350 nm target depth. A linear response occurred during the early unloading branch, and it was over this region that the indentation elastic modulus was estimated. It is observed from the graph that complete unloading was initiated when the residual loads reached 10% of the corresponding peak loads. A few curves (distinguished by dashed lines) exhibited ultimate deformations well exceeding those of other samples, possibly due to the presence of micropores or weak regions under the tip of the indenter. A few others also showed irregularity with apparent shoulders over the loading region, which could have been caused by a fracture or collapse of the surrounding solid structure during loading [17]. These irregular responses represented only about 5–10% of the overall load-indentation depth curves, and this implies that the direct indentation without polishing could provide good quality data for analyses. For the purpose of this study, these outliers were removed.

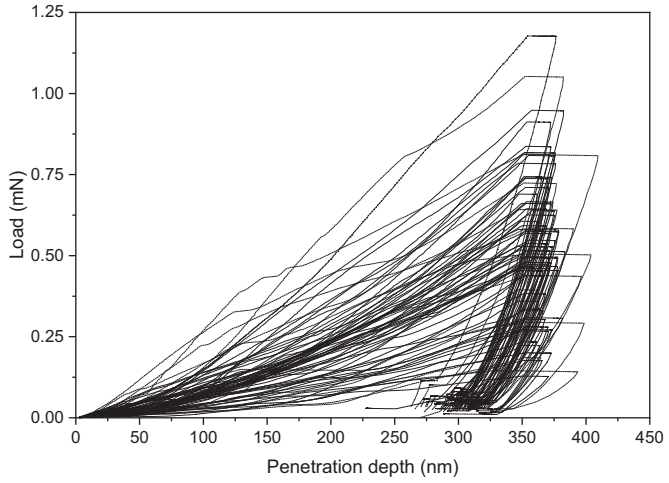

Fig. 5. Load-indentation depth for C-S-H (A0) under 11% RH (RH11), 95 MPa pressure (P1), and 30 min holding time (T30) - (A0-RH111-P1-T30).

3.3.2. Influence of conditioning

Relative frequency plots of elastic modulus data from nanoindentation are given in Fig. 6 for C-S-H and C-A-S-H samples conditioned under freeze-drying, 11%, and 75% RH. All the compacts were prepared with a target or apparent pressure of 95 MPa and a holding time of 30 min. The average elastic modulus and standard deviation values for the individual data sets are also shown in Fig. 6. It is observed that no significant difference in the average elastic modulus for samples conditioned under freeze-drying and 11% RH, attributable to the similar adsorbed moisture content and the resulting similar compressibility under pressure. On the other hand, increasing conditioning RH resulted in an increase in elastic modulus data due to: (i) the formation of denser compacts as enhanced by attraction or sliding of C-(A-)S-H sheets or globules as aided by the presence of moisture [36], and (ii) saturation of nanopores which could reduce the compressibility of the C-(A)S-H matrix. C-A-S-H generally exhibited higher modulus as compared to that of C-S-H under the same conditioning environment. Considering that the micro-morphology of C-(A-)S-H is slightly different [64], the higher modulus of C-A-S-H at microscale under the same conditioning environment could be mainly ascribed to its enhanced compactibility (to be discussed in Section 3.5) and intrinsic mechanical properties at the atomic-nano scale. Pore-free high-pressure X-ray diffraction (XRD) study demonstrated that the cross-linking sites in C-A-S-H synthesized at 80 °C enhanced its mechanical properties, particularly along the c-axis [7]. Also, the EDX scan applied on the surface of pressed compacts revealed that the measured Ca/(Al + Si) and Al/(Al + Si) closely followed the stoichiometric values (Table A in Appendix A as Supplementary information). Of note, it is not the phase chemistry but its implied properties (cross-linking, morphology, packing, etc.) that contributed to the observed micromechanical performance of the C-(A-)S-H compacts.

3.3.3. Influence of holding time

Due to similar characteristics of the test data, relative frequency plots for elastic modulus data of the remaining C-(A-)S-H compacts were not supplied here and instead placed in Appendix A of the Supplementary information. Relative frequency plots of elastic modulus results for C-S-H compacts conditioned at 11% RH, pressed to 95 MPa under holding times of 0 and 60 min are given in Fig. A.2. For easy reference to readers, a summary of the average modulus values at 350 nm obtained from the Basic method and averaged over 300–400 nm from the CSM method are given in Fig. 7. The corresponding error bars of one standard deviation are also given in the graph. It is revealed that a longer holding time increased the elastic modulus of the compacts. Under the same conditioning environment, the average elastic modulus values for C-S-H samples were found to be 5.0, 5.7, and 6.7 GPa for holding times of 0, 30, and 60 min, respectively. The enhanced modulus under a longer holding time was attributed to an increase in the packing density resulting from creep and densification of the matrix under a sustained pressure. A similar densification response to holding time was observed for Al_2O_3 powder of different particle sizes [65].

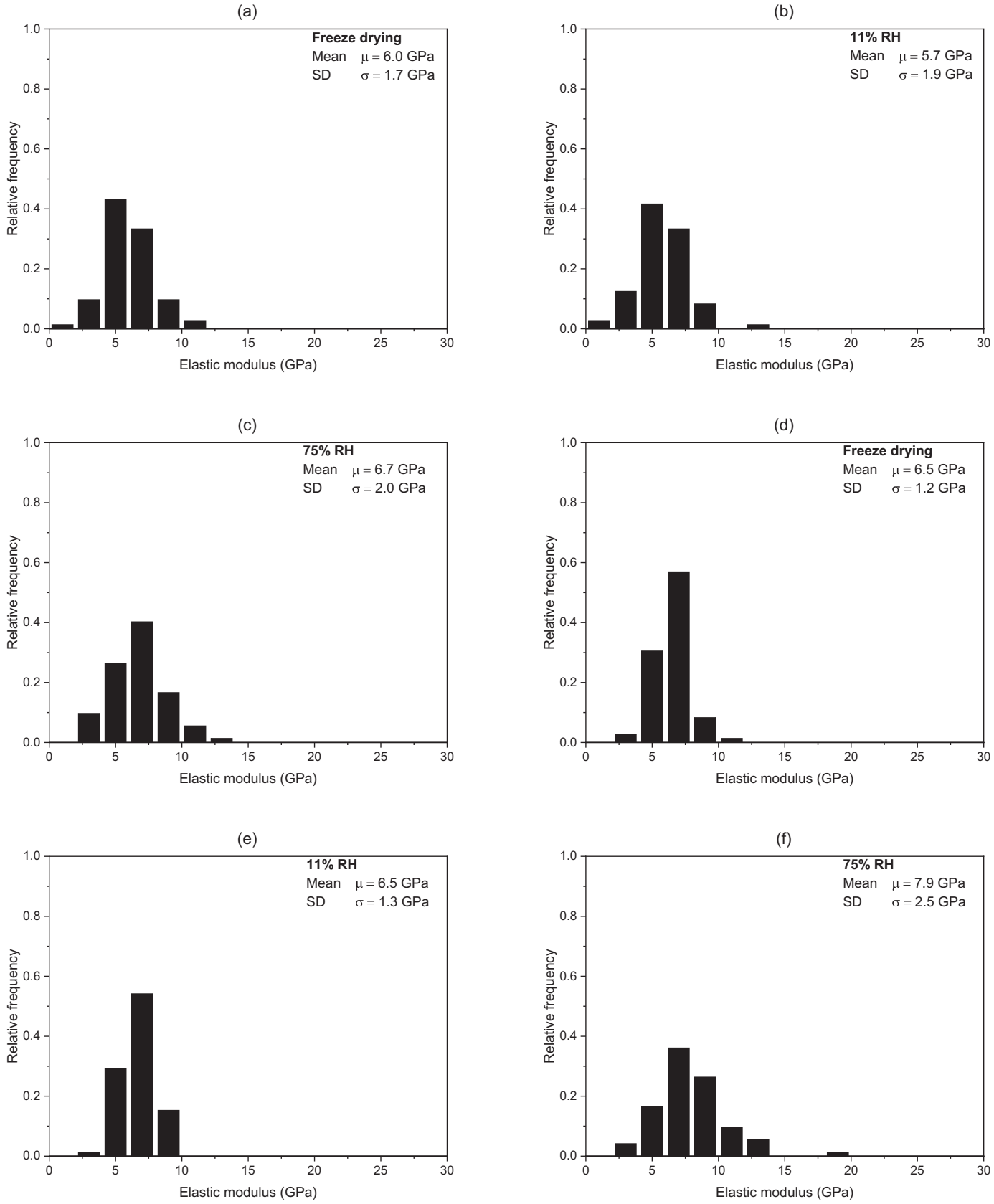

Fig. 6. Elastic modulus from Basic method for C-(A-)S-H samples prepared under 95 MPa pressure (P1) and 30 min holding time (T30): (a) C-S-H (A0) under as-received condition (VA) - (A0-VA-P1-T30), (b) C-S-H (A0) under 11% RH (RH11) - (A0-RH11-P1-T30), (c) C-S-H (A0) under 75% RH (RH75) - (A0-RH75-P1-T30), (d) C-A-S-H (A1) under as-received condition (VA) - (A1-VA-P1-T30), (e) C-A-S-H (A1) under 11% RH (RH11) - (A1-RH11-P1-T30), and (f) C-A-S-H (A1) under 75% RH (RH75) - (A1-RH75-P1-T30).

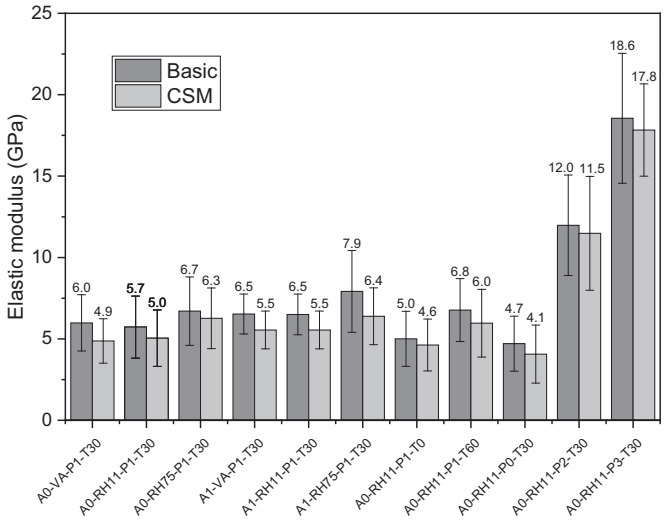

Fig. 7. Comparison of average modulus data from both Basic and CSM methods.

3.3.4. Influence of pressing pressure

Relative frequency plots of elastic modulus data for C-S-H compact samples conditioned at 11% RH, pressed to 50, 200, and 300 MPa under a holding time of 30 min is given in Fig. A.3. For completeness, the results for A0-RH11-P1-T30 obtained from the compact pressed to 95 MPa is also reproduced here. It is observed that increasing pressure in preparing the compacts also increased the elastic modulus values, attributed to the densification of the matrix under the higher applied pressure levels. Interestingly, the data exhibited a wider spread with increasing pressure. The standard deviation increased from 1.7 to 4.0 GPa when the pressure increased from 50 to 300 MPa. It is postulated that when the matrix became more densified, the modulus response would be more sensitive to any inherent defect such as porosity or weak zones, leading to a higher variation in the modulus data. Despite the standard deviation spread, a single slightly-skewed distribution still held for each respective compact, indicating the increase in the elastic modulus was mainly attributed to the matrix densification.

A correlation between the compact density (ρ), the target pressures applied in making the compacts, and the elastic modulus values is plotted in Fig. 8(a) and (b). It is revealed that the compact density increased yet at a decreasing rate with the applied pressure. Inversely, the elastic modulus values increased at an exponential rate with the compact density. An exponential function was used to fit the data to yield a relationship between the elastic modulus and compact density, and an R^2 value of 0.99865 was achieved. As the y-intercept was not set to zero, the relationship would only hold over a density range of 0.8–1.6 g/cm^3. It is also noted that the modulus obtained at the 95 MPa pressure level and 11% RH corresponded to very low density (VLD) C-(A-)S-H with a reported modulus of 7.5 ± 2.0 GPa as observed in [36]. Though, the values obtained from the porous C-(A-)S-H compacts here were lower than those from high-pressure X-ray diffraction (HP-XRD) [7,66], even after accounting for the Poisson effect. It is postulated that the high hydrostatic pressure level used to derive the bulk modulus in these two studies [7,66] induced a stress-strain response at an atomic level without the influence of porosity (> 1 nm) and hence would naturally lead the much higher observed modulus values. Also, contrary to a multi-modal distribution of the elastic modulus for C-S-H as reported in other studies [29,36], a single-modal distribution was observed due to the use of phase-pure materials. The observed single-modal distribution potentially implies that peaks previously assigned to synthetic C-(A-)S-H of different densities [36] could potentially be C-(A-)S-H intermixed with other impurities as evidenced by the decomposition of $Ca(OH)_2$ between 400 and 500 °C in the TGA results of the sample used in that study.

3.3.5. Influence of test parameters

Relative frequency plots of elastic modulus results for A0-RH11-P1 with a holding time of 30 min and under strain rates of 0.025 and 0.1 s^{-1} are shown in Fig. A.4. The results showed that varying strain rates had no noticeable influence on the elastic modulus. The corresponding average elastic modulus remained almost constant at 5.6, 5.6, and 5.7 GPa for strain rates of 0.025, 0.1, and 0.05 s^{-1}, respectively. The findings imply that the mechanical properties of C-(A-)S-H is not dependent on the loading rates in the range of 0.025 to 0.1 s^{-1} when otherwise the tensile and compressive strengths of concrete are known to increase with increasing strain rates [67]. An absence of this characteristic within the C-(A-)S-H compacts could be attributed to either a relatively low strain rates implemented in this study or inherent strain-rate independence of C-(A-)S-H, which requires further investigation.

3.3.6. C_3S paste indentation results

In general, the hydration of C_3S mainly forms C-S-H and $Ca(OH)_2$ [68,69], while the presence of unreacted C_3S and $CaCO_3$ due to carbonation would also be expected in the matrix system. The relative frequency plot for elastic modulus results of the hydrated C_3S paste sample is given in Fig. 9. A total of 225 points were acquired. Deconvolution was performed using Gaussian fit, and the deconvoluted distributions with corresponding distribution means and areas (in

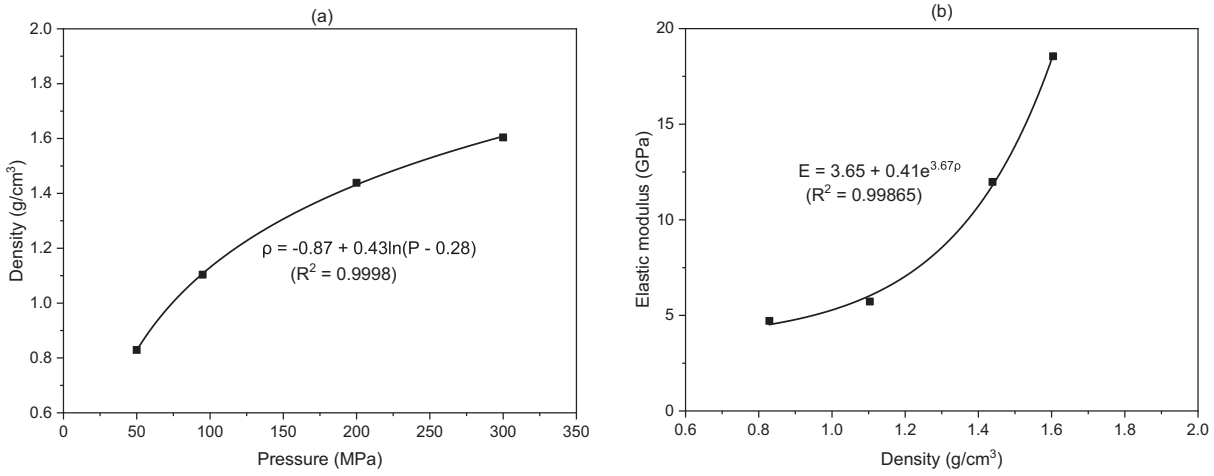

Fig. 8. Correlation between pressure, density, and elastic modulus for C-S-H (A0) samples conditioned under 11% RH: (a) density versus applied pressure, and (b) average elastic modulus versus density.

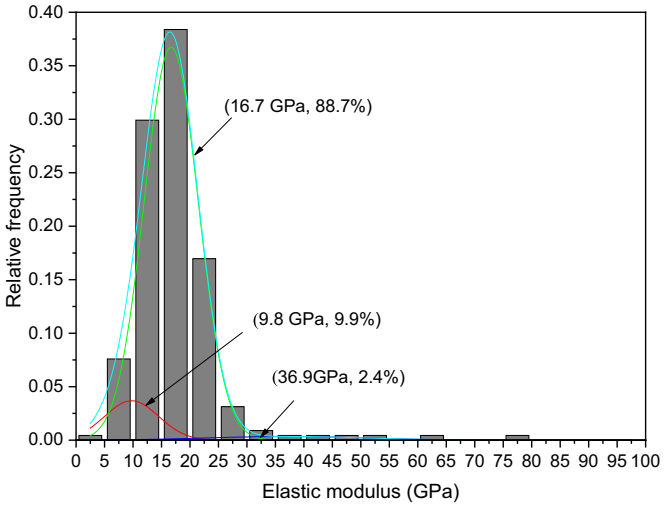

Fig. 9. Elastic modulus for C_3S paste under the Basic method.

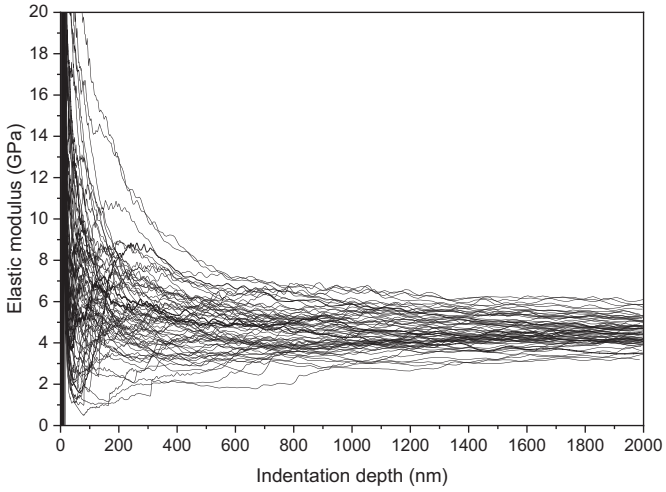

Fig. 10. Modulus-indentation depth response for C-S-H (A0) under 11% RH (RH11), 95 MPa pressure (P1), and 30 min holding time - (A0-RH11-P1-T30) under the CSM method.

brackets) are also shown in Fig. 9. The main distribution with an average elastic modulus 16.7 GPa could be assigned to low-density C-S-H [14,54]. The small particle size of the C_3S powder (< 5 μm as observed by SEM) and the high water-to-binder ratio could have prevented the formation of HD C-S-H as noted by other researchers [14,15]. The other two phases with average elastic modulus values of 9.8 and 36.9 GPa could be associated with C-S-H regions containing micropores and $Ca(OH)_2$ [70], respectively. Despite the high content of $Ca(OH)_2$ within the matrix system as found from the TGA results, its low area distribution could mean that $Ca(OH)_2$ and C-S-H co-existed as microcomposites which preferentially form at high water-to-binder ratio [25]. Thus, the C-S-H phase with the reported modulus of 16.7 GPa could potentially be these microcomposites. SEM analysis of the fractured surface of the C_3S sample (not shown here) confirmed the intermixing of $Ca(OH)_2$ and C-S-H. An absence of elastic modulus values in the range of 125–145 GPa for C_3S [13,71] implied that the small particle size and long curing time led to full hydration of the C_3S sample adopted in this study.

It is also important to note that the phase modulus data obtained from the C_3S paste were generally much higher than the synthetic C-(A-)S-H. At a pressing pressure of 200 MPa, the average modulus for synthetic C-S-H was found to be only 12.0 GPa, less than the 16.7 GPa for the low-density C-S-H obtained from the C_3S paste. The deviation could also be attributed to a difference in the inherent phase bonding, porosity, chemical compositions, and presence of $Ca(OH)_2$ intermixed in the system. Likewise, it has been established that the stiffness of C-(A-)S-H in hydrated cement pastes is dependent on various parameters such as its packing density [72], relative Ca content or Ca leaching [14,15], Ca/Si molar ratio [27] and impurity inclusion [21,25,73].

3.4. Nanoindentation results from CSM method

3.4.1. Modulus-indentation depth response

Typical elastic modulus-indentation depth responses at all indentation locations for A0-RH11-P1-T30 tested under the CSM method are depicted in Fig. 10. A notable dispersion of elastic modulus values during the initial indentation stage was observed, and that could be attributed to an analytical instability as the indenter tip started to penetrate into the sample. The data converged when the indentation depth was > 300 nm, and the data spread further reduced as the indentation depth increased. Such an indentation depth-modulus response from the CSM method could be used as a tool to investigate phase uniformity in non-homogeneous materials. The modulus corresponding to a specific or a range of indentation depth could be found, and frequency plots similar to those derived from the Simple method could be obtained.

3.4.2. Influence of conditioning

Relative frequency plots of elastic modulus data averaged over an indentation depth between 300 and 400 nm from the CSM method are given in Fig. A.5 for C-S-H and C-A-S-H samples conditioned under freeze-drying, 11% RH, and 75% RH. The average elastic modulus and standard deviation values for the individual nanoindentation tests are also given in the graph. Similar to the trend observed for the Basic method, it is revealed that increasing conditioning RH resulted in an increase in elastic modulus data for both C-S-H and C-A-S-H samples. The results also confirmed that under the same conditioning RH, C-A-S-H generally yielded compacts of higher modulus values, attributed its enhanced cross-linking and compactibility as discussed earlier. In comparison to the modulus data obtained from the Basic method at the penetration depth of 350 nm, the CSM technique generally produced lower elastic modulus values. Under the CSM method, the indentation system and sample contacts are governed by dynamic modeling, and the contact stiffness was shown to depend on a number of machine parameters including damping, load frame stiffness and support spring stiffness [39]. The set values of the parameters could contribute to the resulting discrepancy. Also, the small harmonic displacement amplitude of 2 nm provides a small unloading region for the contact stiffness fitting, and this could potentially be another source of error. The initial unloading branch from the load-indentation depth curve is not purely elastic, as observed by other researchers [9].

Fig. 11 plots the elastic modulus values averaged at every 100 nm interval up to a total indentation depth of 2000 nm for A0-VA-P1-T30, A0-RH11-P1-T30, and A0-RH75-P1-T30. Error bars represented by one standard deviation for A0-VA-P1-T30 were also shown on the graph. It is confirmed that due to the initial instability, the average modulus data were generally high with larger standard deviations during the early stage of loading. Convergence was observed beyond a penetration depth of 300 nm, thus validating the target penetration depth of 350 nm as adopted in the Basic method. Consistent with the data obtained from the Basic at 350 nm method and the CSM technique with modulus averaged over 300–400 nm, throughout the indentation depth both A0-VA-P1-T30 and A0-RH11-P1-T30 exhibited similar average elastic modulus values while A0-RH75-P1-T30 achieved higher modulus values due to an enhanced compactibility of A0 sample under high humidity conditioning. A similar trend was also observed for A1 samples, although the data are not presented here.

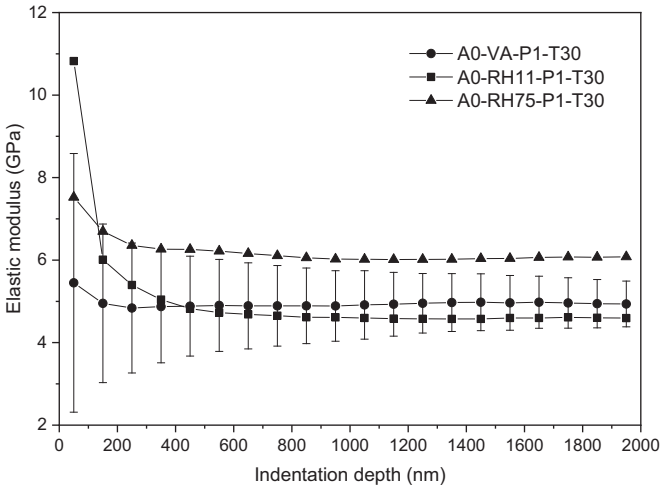

Fig. 11. Average modulus data with indentation depth for C-S-H (A0) under as-received condition (VA), 95 MPa pressure (P1), and 30 min holding time (T30) - (A0-VA-P1-T30); C-S-H (A0) under 11% RH (RH11), 95 MPa pressure (P1), and 30 min holding time (T30) - (A0-RH11-P1-T30), and C-S-H (A0) under 75% RH (RH75), 95 MPa pressure (P1), and 30 min holding time (T30) - (A0-RH75-P1-T30) from CSM method.

3.4.3. Influence of indentation parameters

Fig. 12 summarizes the indentation depth-average elastic modulus relationship for the A0 sample tested under different levels of loading frequency and strain rate. The elastic modulus values were obtained from the CSM method and averaged at every 100 nm interval. Of note is the fact that A0-RH11-P1-S1 and A0-RH11-P1-S1-F1 are the same samples under the same test condition (strain rate of 0.05 s^{-1} and frequency of 45 Hz). It is observed that oscillation frequencies between 22.5 and 60 Hz had no noticeable influence on the modulus results beyond the stability penetration depth of approximately 300 nm. Also, the strain rates between 0.025 and 0.1 s^{-1} had no statistical significance on the mechanical properties of the C-(A-)S-H compacts. Increasing the strain rates was observed to cause a slight increase and decrease in the average modulus values. Consistent with the findings from the Basic method, the mechanical properties of C-(A-)S-H are inferred to be strain-rate independent for a small strain rate window between 0.025 and 0.1 s^{-1}. Though, strain rate dependency of other types of materials, including bone [74], alloy [75], and polymer [76],

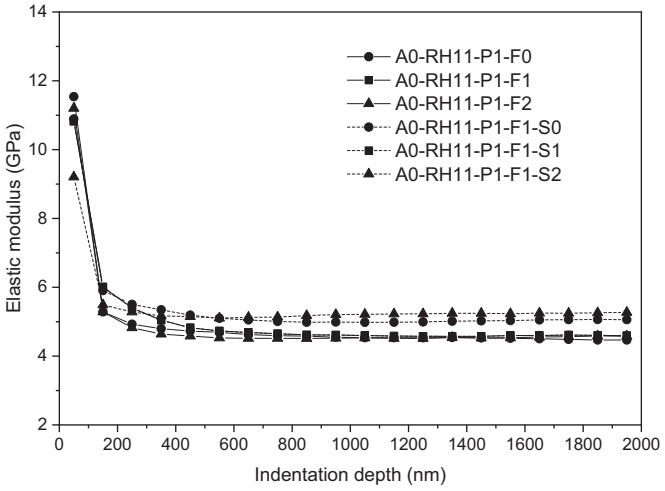

Fig. 12. Average modulus data with indentation depth for C-S-H (A0) under 11% RH (RH11), 95 MPa pressure (P1) - (A0-RH11-P1-F0) - with loading frequency of 22.5 Hz (F0), 45 Hz (F1), and 60 Hz (F2), and loading rate of 0.025 s^{-1} (S0), 0.05 s^{-1} (S1), and 0.1 s^{-1} (S2).

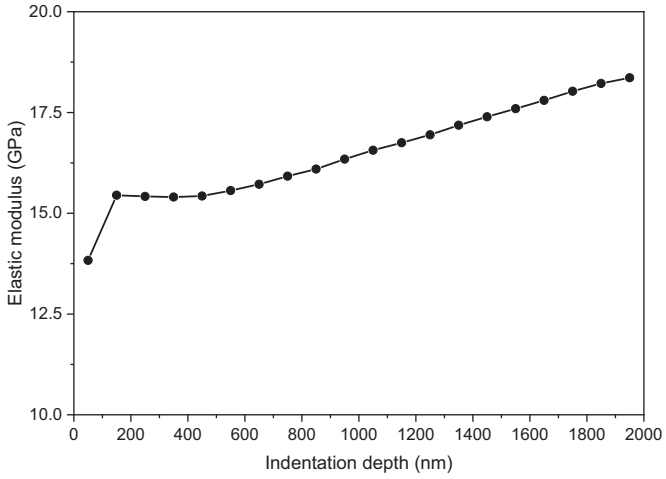

Fig. 13. Average modulus data with indentation depth for C_3S paste.

were observed at larger strain rate range or magnitude.

3.4.4. C_3S paste indentation results

The distribution of elastic modulus values averaged over an indentation depth of 300–400 nm for the C_3S paste sample was moved to Fig. A.6 of Appendix A due to its similar characteristics to the sample tested under the Basic method. The deconvoluted distributions obtained with Gaussian fitting are also shown with corresponding distribution means and areas. Phase modulus values of 9.7, 16.1, and 34.1 GPa were identified and could be assigned to C-S-H regions with micropores, C-S-H intermixed with $Ca(OH)_2$, and $Ca(OH)_2$, respectively, as discussed in Section 3.3.6. At the target penetration depth of 350 nm, the modulus data obtained from both the Basic and CSM methods for the hydrated C_3S sample were in good agreement, consistent with the trend noted in the C-(A-)S-H compacts. However, the average elastic modulus values (calculated over 100 nm intervals) for the C_3S sample were observed to increase with the indentation depth, as demonstrated in Fig. 13. A similar upward trend was also observed for indentation on the undisturbed (mold face) or fractured (uneven) surfaces. Thus, the phenomenon could not be attributed to the surface roughness or possible surface disturbance during polishing. The influence of strain energy gradient within the interaction volume [34] or confinement afforded by the surrounding material could neither be a factor as such an upward trend was not observed for the compressed C-(A-)S-H samples (Fig. 11). One plausible explanation is that as the indentation depth increased, the interaction volume beneath the indenter's tip would accordingly become larger at a faster rate than the depth and the projected contact area. The larger $Ca(OH)_2$ phase of higher elastic modulus would be more engaged and act as stiffening elements, thus resulting in an increase in the observed elastic modulus values. However, further investigation is required to elucidate the phenomenon.

3.4.5. Comparison of modulus values from Basic and CSM methods

It is revealed in Fig. 7 that the average CSM modulus data were generally lower than the values obtained from the Basic method. Also, for the same conditioning, samples prepared with A1 led to higher modulus values as compared samples prepared with A0 due to enhanced cross-linking of C-(A-)S-H with the inclusion of Al and possibly a different morphology conducive to compaction. Also, higher holding time, relative humidity, and compressing pressure to make compacts also increased the mechanical properties of the C-(A-)S-H compacts. The finding re-affirmed the various factors that could influence the nanoindentation data of C-(A-)S-H compacts, and it is important that these parameters are carefully fine-tuned to ensure the consistency of the test data.

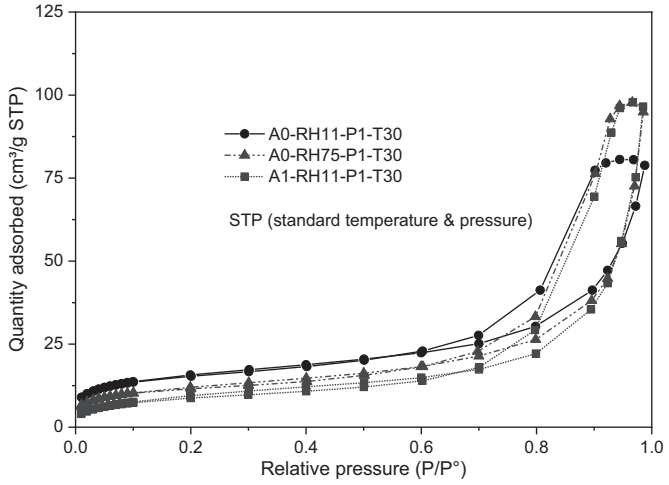

Fig. 14. Adsorption-desorption curves for C-S-H (A0) under 11% RH (RH11), 95 MPa pressure (P1), and 30 min holding time (T30) - (A0-RH11-P1-T30); C-S-H (A0) under 75% RH (RH75), 95 MPa pressure (P1), and C-A-S-H (A1) under 11% RH (RH11), 95 MPa pressure (P1), and 30 min holding time (T30) - (A0-RH75-P1-T30).

3.5. N_2 adsorption results

Adsorption-desorption isotherms for three selected samples (A0-RH11-P1-T30, A0-RH75-P1-T30, and A1-RH11-P1-T30) are shown in Fig. 14. The vertical axis represents the amount of N_2 absorbed per gram of the solid materials (at standard temperature and pressure), while the horizontal axis denotes the relative pressure (P/P_o). Hysteresis loops corresponding to Type IV isotherms [77] are observed and associated with capillary condensation in mesopores of internal width between 2 and 50 nm [57]. The curvature observed toward the end region of the isotherms implies that a condensation limit was reached before larger pores were filled with gaseous N_2 and thus a complete pore size distribution of the compacts using the N_2 adsorption method could not be made. One useful parameter is the specific surface area (SSA) that could be derived from the Brunauer-Emmett-Teller (BET) theory, as the method relies on the monolayer adsorption capacity of porous materials [77]. The SSA values derived from the linearity of the isotherms with the P/P_o range of 0.05–0.30 were found to be 56.4, 43.4, and 35.9 m^2/g for A0-RH11-P1-T30, A0-RH75-P1-T30, and A1-RH11-P1-T30, respectively. In comparison, C-S-H and C-A-S-H powder samples were found to have SSA of 96.9 m^2/g and 82.6 m^2/g, respectively. The smaller SSA of A0-RH75-P1-T30 as compared to A0-RH11-P1-T30 confirmed that the higher conditioning RH led to a denser compact. Also, compressing induced matrix densification and consequentially reduced the SSA of the compacts relative to that for the uncompressed powder. Relative to A0-RH11-P1-T30, A1-RH11-P1-T30 was found to have a smaller SSA and exhibit a greater percentage reduction in SSA when transformed from powder to compact, implying that the morphology of A1 was more yielding to compression at 11% RH. It follows that the superior mechanical properties of A1 could be attributed to both a more compressible morphology, in addition to an enhanced cross-linking of C-(A-)S-H products with the incorporation of Al [7].

3.6. SEM results

Fig. 15 showed BSE images of indentation map and single indentation for A0-RH11-P1-T30 and A0-RH11-P3-T30 tested under the CSM technique to a target penetration depth of 2000 nm. Fig. 15(b) and (c) revealed that the grain structure of C-S-H remained more apparent in A0-RH11-P1-T30 prepared with a pressing pressure of 95 MPa in comparison to A0-RH11-P3-T30 prepared with 300 MPa. The lower compaction and densification in A0-RH11-P1-T30 contributed to its lower elastic modulus data. It is also revealed that all indented regions were well defined with no material pileup and presence of cracks at the corners of the indents, thus confirming that the target penetration depth of 2000 nm would not induce microstructural damage which could adversely affect the validity of the test data. It follows that the distribution of the modulus data could be due to the porosity inherent in the C-S-H compacts. Over the void regions, a reduction in the actual contact surface area would lead to a reduction in the applied load at the corresponding penetration depth, consequentially resulting in the lower elastic modulus values.

4. Discussion

4.1. Compressibility and moisture content

The nanoindentation results showed that higher conditioning relative humidity (RH) led to higher elastic modulus data, attributable to an enhanced compactibility of the powder. Heckel plots for A0 and A1 conditioned at 11% and 75% RH are given in Fig. 16. The plots confirmed C-(A-)S-H followed Type A material according to a classification by Hersey and Rees [51,78], where the compaction obeys a linear relationship with the applied pressure. The slopes over the middle regions of the curves are constant and represent the compaction behavior of the powder, with higher constants associated with susceptibility to plastic deformation under pressure. Linear curve fitting over regions demarcated by short vertical lines was used to find the constants, and the results (also graphically presented in Fig. 16) showed that the slope of A0 increased from 0.0048 under 11% RH to 0.069 under 75% RH, thus confirming a higher compressibility of the powder when conditioned under a higher RH. A similar trend also applied for A1 under 11% and 75% RH. The higher slopes of A1 under 11% and 75% RH as compared A0 at the corresponding RH level indicate that A1 was more compressible, possibly through sliding of globules, to create compacts of higher elastic modulus under nanoindentation. Thus, both cross-linking and enhanced densification contributed to the improved elastic modulus of the C-A-S-H compact samples. The effects of Al incoporation on the inherent mechanical properties of C-(A-)S-H were investigated in previous studies where the incorporation was shown to enhance cross-linking of C-A-S-H and its c-axis modulus [7,37]. Though, it is not clear if such a conclusion could be applied to C-(A-)S-H of other stoichiometries.

4.2. Parameters influencing nanoindentation results for pressed powder and cement-based paste

It has been shown that a multitude of factors could influence the elastic modulus data derived from the nanoindentation of C-(A-)S-H compacts produced through pressing. First, conditioning under increasing the relative humidity level led to a higher moisture content being adsorbed on the C-(A-)S-H structure, more saturated nanopores, improved compactibility, and ultimately an increase in the elastic modulus values. In the sample preparation, longer holding time, and higher target pressure to form compacts also enhanced microstructural re-arrangement, densification, and the elastic modulus data. During unloading to extract the pressed compacts, friction also existed between the die wall, sample and steel endplates or pellets. The friction depends on the axial stress, sample aspect ratio and transfer ratio [79]. Load versus displacement curves (unloading) for selected samples are shown in Fig. 17, and the average friction or pull-out force values were found to be in the range of 400–450 N for the powder samples investigated in this study, deeming a comparative study between them feasible. The presence of the friction implied that the effective pressures on the compacts were lower than the target pressure levels, and the presented indentation data underestimated the elastic modulus as compared to the case that the friction could be eliminated. The application of lubricant [49,80] and the use of smaller quantities of the powder could all

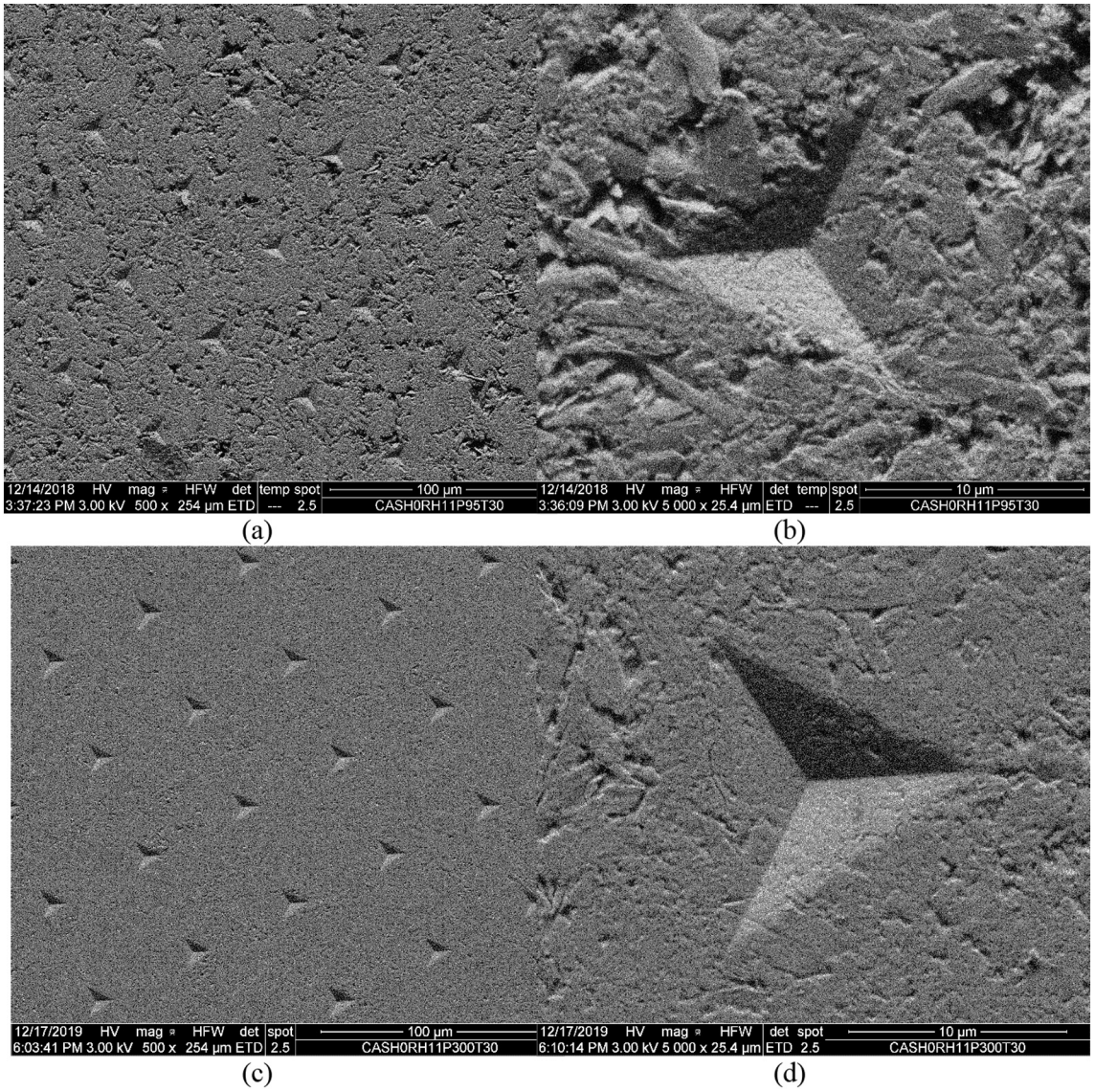

Fig. 15. BSE images showing (a) indentation map, (b) zoomed-in region of a single indentation for C-S-H (A0) under 11% RH (RH11), 95 MPa pressure (P0), and 30 min holding time (T30) - (A0-RH11-P1-T30), (c) indentation map, and (d) zoomed-in region for C-S-H (A0) under 11% RH (RH11), 300 MPa pressure (P1), and 30 min holding time (T30) - (A0-RH11-P3-T30).

lead to a reduced wall-compact friction and a subsequent increase in the observed elastic modulus values. Also, it has been shown that the testing techniques could affect the elastic modulus of the C-(A-)S-H compacts. The CSM method tended to underestimate the elastic modulus in comparison with the Basic method. For sample surfaces achieved with endplates of mirror finish, it was observed that a convergence of data could only be achieved at an indentation depth > 300 nm. On the other hand, for the polished C_3S paste sample, a convergence did not seem to exist at all even up to an indentation depth of 2000 nm, possibly attributable to the combined influence of multiple phases and increasing interaction volume present underneath the indenter's tip. The use of compressed compacts eliminated the requirement to polish the sample. Yet, this is not the case for paste samples, which require careful preparation to minimize the surface roughness, which was found to adversely influence the convergence of material properties derived from nanoindentation [26]. A comprehensive study using Atomic Force Microscopy (AFM) showed that for statistical indentation results to converge, the average indentation depth of the first peak should be > 5 times the surface roughness [26]. A larger target penetration depth could be implemented to avoid the influence of the surface roughness. However, in the case of a matrix comprising multiple micro phases, isolation of their micromechanical signatures is only possible when the linear size of the interaction volume is less than the homogeneous isotropic domain of each single phase [23].

4.3. Multi-scale and multiphase elastic modulus in cement system

According to Jennings's CM-II model [47], the nanostructure of C-S-H in cement could be described as colloids of globules containing solid C-S-H, pores and water. In addition to the intrinsic intra and interlayer space, the hierarchical pore system in packed globules is also composed of intraglobular pores (IGP) (< 1 nm) which are void between sheets, small gel pores (SGP) (1–3 nm) in between packed globules, and large gel pores (LGP) (3–12 nm) within flocs of the globules [47,55]. In a paste system, capillary (100 nm size range) and inherent microporosity also exist [81]. With an interaction volume of 3–4 times the indentation depth [15,34], the indentation elastic modulus values in the range of 4.1–18.6 GPa obtained from the current study with the indentation depth ranging from 0 to 2000 nm would reflect the aggregate effect of all the pore system. On the other hand, the bulk modulus data from

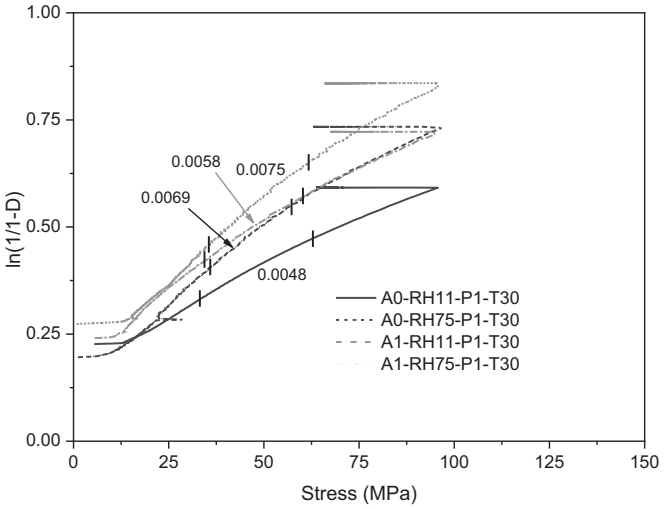

Fig. 16. Heckel plots for C-S-H (A0) and C-A-S-H (A1) samples conditioned under 11% and 75% RH.

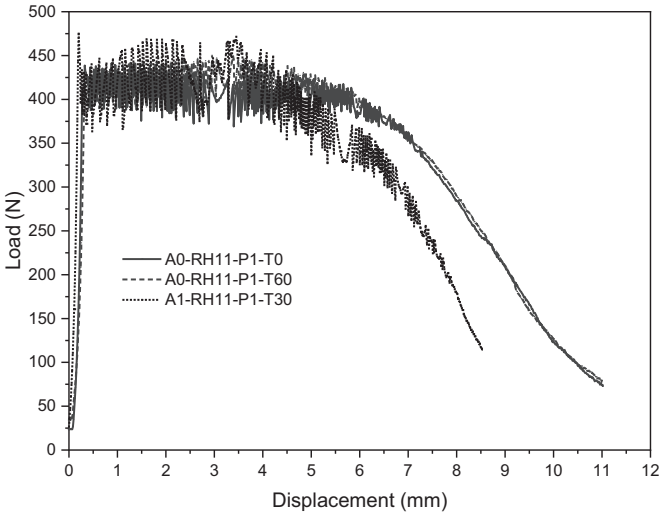

Fig. 17. Unloading curves for C-S-H (A0) under 11% RH (RH11), 95 MPa pressure (P1), and 0 min holding time (T0) - (A0-RH11-P1-T0); C-S-H (A0) under 11% RH (RH11), 95 MPa pressure (P1), and 60 min holding time (T60) - (A0-RH11-P1-T60), and C-A-S-H (A1) under 11% RH (RH11), 95 MPa pressure (P1), and 30 min holding time (T30) - (A1-RH11-P1-T30).

high pressure X-ray diffraction (HP-XRD) by Geng et al. [7,66] were derived by applying a high hydrostatic pressure on C-(A-)S-H in a methanol-ethanol pressure medium which is able to penetrate into pores of 1 nm. High bulk modulus values (36.0–77.4 GPa) were reported and correlated with the compressibility of the intra and interlayer space and thus would be more representative of the intrinsic behavior of the material. Atomic force microscopy (AFM) was used to probe the elastic modulus of C-S-H [82]. With an indentation radius of approximately 40 nm, the involvement of the interspersed voids and multiple phases could be disregarded and the achieved elastic modulus from AFM is thus also intrinsic of C-S-H. Indeed, the reported elastic modulus values based on the technique were between 15 and 80 GPa [82] and were consistent with the range obtained from HP-XRD.

The results also indicated that C-S-H (as a composite of $Ca(OH)_2$) in the hydrated C_3S paste exhibited a significantly higher elastic modulus as compared to C-S-H compacts prepared at pressures < 200 MPa. At a higher pressure of 300 MPa, the C-S-H compact afforded an elastic modulus of 18.6 GPa, more than the 16.7 GPa value obtained from the C_3S paste. It follows that compacts produced from C-(A)-S-H powder could be used to simulate intrinsic C-(A)-S-H in hydrated cement paste, provided that the packing density is matched by choosing the right level of pressure in the compact preparation. Though, the compactibility and the resulting density of C-(A-)S-H compacts is inherently dependent on the moisture state of C-(A-)S-H globules [47], as confirmed in this study. Also, the existence of pure C-(A-)S-H in cement pastes could be a rarity. It has been claimed that peak distribution of the low density (LD) and high density (HD) C-(A-)S-H in cement pastes could be deconvoluted at relatively low indentation depth (200–300 nm) as long as the linear size of hydration products is > 2000–3000 nm [34]. However, based on focused-ion beam nanotomography, such large sizes of single-phase domain may not occur in hydrated cement pastes and hence the observed elastic modulus could only be associated with phase composites [23,24]. An intermixing of other impurities such as $Ca(OH)_2$ nanocrystallites were earlier shown to be present within the C-S-H matrix and led to a significant increase in its elastic modulus [25]. To overcome this ambiguity of the existence of multiple phases in cementitious composites, an automated coupling of nanoindentation and energy dispersive spectroscopy (EDS) was introduced and the technique successfully allowed a chemo-mechanical linkage of phases in cement-based materials [21,31], high volume natural pozzolan concrete [32], and high-performance glass concrete [83]. The complexity of the scale and phase associated with the elastic modulus data from the nanoindentation of cement pastes would ultimately require careful engineering interpretation to understand its influence on the macro properties of concrete.

5. Conclusions

Nanoindentation has become one of the most commonly used techniques to characterize the micromechanical signature of materials. In this study, nanoindentation was performed on compacts made from compressed C-(A-)S-H powder with Al/(Al + Si) = 0 and 0.1. The influence of various factors, including conditioning environment, pressure level, pressure holding time adopted in powder compression to produce the compacts, and nanoindentation test parameters on the resulting micromechanical properties was investigated. C_3S paste was also used for comparison. Based on the results and discussion provided, the following can be concluded:

- C-(A-)S-H compacts produced from pressing with mirror-finished endplates could be directly used for nanoindentation with no further polishing requirements. Normal distribution and convergence of test data could be attained with an indentation depth > 300 nm.
- By adopting a sinusoidal load at a selected frequency during loading, the Continuous Stiffness Method (CSM) was able to continuously capture the micromechanical properties of the indented materials throughout the indentation depth as compared to end-point measurement obtainable with the Basic method.
- A single-modal distribution was observed for the studied phase-pure materials due to an absence of impurities such as $Ca(OH)_2$ with low Ca/Si ratios.
- For C-(A-)S-H pellets, both the Basic and CSM methods produced a similar trend of modulus data despite a slight underestimation with the CSM method, attributable to machine parameters including damping, load frame stiffness and support spring stiffness, which could be calibrated to achieve a result consistency. The micromechanical properties of C-(A-)S-H were found to be independent of strain rate rates in the range of 0.025 to 0.1 s^{-1} and loading frequency, some of the control parameters in the CSM method.
- On the other hand, the conditioning environment and sample preparation procedure were found to have a significant influence on the indentation results. Increasing conditioning relative humidity (RH), pressure level, and holding time improved consolidation, reduced porosity, and enhanced the resulting elastic modulus. An exponential relationship was observed between the compact density

and the resulting elastic modulus.

- The incorporation of Al in the framework of C-A-S-H increased its elastic modulus, possibly due to cross-linking within its fundamental structure and an improved compactibility of the C-A-S-H globules.
- In comparison to C-(A-)S-H compacts, hydrated C_3S paste yielded higher elastic modulus, mainly attributable to a difference in phase bonding, packing density, chemical composition, and a possible presence of $Ca(OH)_2$ within the C-S-H matrix.

The study demonstrated the various factors that could influence micromechanical properties characterized by nanoindentation of C-(A-)S-H compacts, and the findings call for prudent sample preparation and selection of test parameters to achieve consistent nanoindentation test data.

CRediT authorship contribution statement

Rotana Hay: Conceptualization, Methodology, Investigation, Writing - original draft, Writing - review & editing, Project administration. **Jiaqi Li:** Methodology, Investigation, Writing - review & editing. **Kemal Celik:** Writing - review & editing, Supervision, Project administration, Funding acquisition.

Declaration of competing interest

The authors declare that they have no known competing financial interests or personal relationships that could have appeared to influence the work reported in this paper.

Acknowledgment

The authors wish to express their gratitude and sincere appreciation to New York University Abu Dhabi for grant number ADHPG-ST254 to make this research possible and to Core Technology Platforms (CTPs) experts, specifically Dr. James Weston and Dr. Liang Li, for guidance with some of the experiment. In addition, this work was supported by the New York University Abu Dhabi Center for Interacting Urban Networks (CITIES), funded by Tamkeen under the New York University Abu Dhabi Research Institute Award CG001 and by the Swiss Re Institute under the Quantum Cities™ initiative.

Appendix A. Supplementary information

Supplementary data to this article can be found online at https://doi.org/10.1016/j.cemconres.2020.106088.

References

[1] H.F.W. Taylor, Cement Chemistry, Thomas Telford, 1997.
[2] C. Famy, A.R. Brough, H.F.W. Taylor, The CSH gel of Portland cement mortars: part I. The interpretation of energy-dispersive X-ray microanalyses from scanning electron microscopy, with some observations on CSH, AFm and AFt phase compositions, Cem. Concr. Res. 33 (2003) 1389–1398.
[3] I.G. Richardson, The calcium silicate hydrates, Cem. Concr. Res. 38 (2008) 137–158.
[4] C.A. Love, I.G. Richardson, A.R. Brough, Composition and structure of C–S–H in white Portland cement–20% metakaolin pastes hydrated at 25 C, Cem. Concr. Res. 37 (2007) 109–117.
[5] C. Li, H. Sun, L. Li, A review: the comparison between alkali-activated slag (Si + Ca) and metakaolin (Si + Al) cements, Cem. Concr. Res. 40 (2010) 1341–1349.
[6] I.G. Richardson, Model structures for C-(A)-SH (I), Acta Crystallogr. Sect. B: Struct. Sci. Cryst. Eng. Mater. 70 (2014) 903–923.
[7] G. Geng, R.J. Myers, J. Li, R. Maboudian, C. Carraro, D.A. Shapiro, P.J.M. Monteiro, Aluminum-induced dreierketten chain cross-links increase the mechanical properties of nanocrystalline calcium aluminosilicate hydrate, Sci. Rep. 7 (2017) 44032.
[8] J.B. Pethicai, R. Hutchings, W.C. Oliver, Hardness measurement at penetration depths as small as 20 nm, Philos. Mag. A 48 (1983) 593–606.
[9] W.C. Oliver, G.M. Pharr, An improved technique for determining hardness and elastic modulus using load and displacement sensing indentation experiments, J. Mater. Res. 7 (1992) 1564–1583.
[10] F. Carrillo, S. Gupta, M. Balooch, S.J. Marshall, G.W. Marshall, L. Pruitt, C.M. Puttlitz, Nanoindentation of polydimethylsiloxane elastomers: effect of crosslinking, work of adhesion, and fluid environment on elastic modulus, J. Mater. Res. 20 (2005) 2820–2830.
[11] S. Gupta, F. Carrillo, C. Li, L. Pruitt, C. Puttlitz, Adhesive forces significantly affect elastic modulus determination of soft polymeric materials in nanoindentation, Mater. Lett. 61 (2007) 448–451.
[12] D.M. Ebenstein, L.A. Pruitt, Nanoindentation of biological materials, Nano Today 1 (2006) 26–33.
[13] K. Velez, S. Maximilien, D. Damidot, G. Fantozzi, F. Sorrentino, Determination by nanoindentation of elastic modulus and hardness of pure constituents of Portland cement clinker, Cem. Concr. Res. 31 (2001) 555–561.
[14] G. Constantinides, F.J. Ulm, K. Van Vliet, On the use of nanoindentation for cementitious materials, Mater. Struct. 36 (2003) 191–196.
[15] G. Constantinides, F.-J. Ulm, The effect of two types of C-S-H on the elasticity of cement-based materials: results from nanoindentation and micromechanical modeling, Cem. Concr. Res. 34 (2004) 67–80.
[16] J. Vanzo, A Nanochemomechanical Investigation of Carbonated Cement Paste (Doctoral dissertation), Massachusetts Institute of Technology, 2009.
[17] C. Hu, Z. Li, Micromechanical investigation of Portland cement paste, Constr. Build. Mater. 71 (2014) 44–52.
[18] G. Constantinides, F.-J. Ulm, The nanogranular nature of C–S–H, J. Mech. Phys. Solids 55 (2007) 64–90.
[19] P. Mondal, S.P. Shah, L. Marks, A reliable technique to determine the local mechanical properties at the nanoscale for cementitious materials, Cem. Concr. Res. 37 (2007) 1440–1444.
[20] C. Hu, Z. Li, A review on the mechanical properties of cement-based materials measured by nanoindentation, Constr. Build. Mater. 90 (2015) 80–90.
[21] W. Wilson, L. Sorelli, A. Tagnit-Hamou, Automated coupling of NanoIndentation and Quantitative Energy-Dispersive Spectroscopy (NI-QEDS): a comprehensive method to disclose the micro-chemo-mechanical properties of cement pastes, Cem. Concr. Res. 103 (2018) 49–65.
[22] S. Gautham, S. Sasmal, Recent advances in evaluation of intrinsic mechanical properties of cementitious composites using nanoindentation technique, Constr. Build. Mater. 223 (2019) 883–897.
[23] P. Trtik, B. Münch, P. Lura, A critical examination of statistical nanoindentation on model materials and hardened cement pastes based on virtual experiments, Cem. Concr. Compos. 31 (2009) 705–714.
[24] P. Lura, P. Trtik, B. Münch, Validity of recent approaches for statistical nanoindentation of cement pastes, Cem. Concr. Compos. 33 (2011) 457–465.
[25] J.J. Chen, L. Sorelli, M. Vandamme, F.J. Ulm, G. Chanvillard, A coupled nanoindentation/SEM-EDS study on low water/cement ratio Portland cement paste: evidence for C–S–H/$Ca(OH)_2$ nanocomposites, J. Am. Ceram. Soc. 93 (2010) 1484–1493.
[26] M. Miller, C. Bobko, M. Vandamme, F.-J. Ulm, Surface roughness criteria for cement paste nanoindentation, Cem. Concr. Res. 38 (2008) 467–476.
[27] F. Pelisser, P.J.P. Gleize, A. Mikowski, Effect of the Ca/Si molar ratio on the micro/nanomechanical properties of synthetic CSH measured by nanoindentation, J. Phys. Chem. C 116 (2012) 17219–17227.
[28] W. Hunnicutt, P. Mondal, L. Struble, Dynamic and quasi-static nanoindentation of CSH and CASH, Spec. Publ. 312 (2016) 1–15.
[29] J.J. Kim, E.M. Foley, M.M.R. Taha, Nano-mechanical characterization of synthetic calcium–silicate–hydrate (C–S–H) with varying CaO/SiO_2 mixture ratios, Cem. Concr. Compos. 36 (2013) 65–70.
[30] W. Zhu, J.J. Hughes, N. Bicanic, C.J. Pearce, Nanoindentation mapping of mechanical properties of cement paste and natural rocks, Mater. Charact. 58 (2007) 1189–1198.
[31] K. J. Krakowiak, W. Wilson, S. James, S. Musso, F.-J. Ulm, Inference of the phase-to-mechanical property link via coupled X-ray spectrometry and indentation analysis: application to cement-based materials, Cem. Concr. Res. 67 (2015) 271–285.
[32] W. Wilson, J.M. Rivera-Torres, L. Sorelli, A. Durán-Herrera, A. Tagnit-Hamou, The micromechanical signature of high-volume natural pozzolan concrete by combined statistical nanoindentation and SEM-EDS analyses, Cem. Concr. Res. 91 (2017) 1–12.
[33] W. Wilson, L. Sorelli, A. Tagnit-Hamou, Unveiling micro-chemo-mechanical properties of C–(A)–S–H and other phases in blended-cement pastes, Cem. Concr. Res. 107 (2018) 317–336.
[34] F.-J. Ulm, M. Vandamme, H.M. Jennings, J. Vanzo, M. Bentivegna, K.J. Krakowiak, G. Constantinides, C.P. Bobko, K.J. Van Vliet, Does microstructure matter for statistical nanoindentation techniques? Cem. Concr. Compos. 32 (2010) 92–99.
[35] Y. Zhou, W. She, D. Hou, B. Yin, H. Chang, J. Jiang, J. Li, Modification of incorporation and in-situ polymerization of aniline on the nano-structure and meso-structure of calcium silicate hydrates, Constr. Build. Mater. 182 (2018) 459–468.
[36] E.M. Foley, J.J. Kim, M.M.R. Taha, Synthesis and nano-mechanical characterization of calcium-silicate-hydrate (CSH) made with 1.5 CaO/SiO2 mixture, Cem. Concr. Res. 42 (2012) 1225–1232.
[37] R.J. Myers, E. L'Hôpital, J.L. Provis, B. Lothenbach, Effect of temperature and aluminium on calcium (alumino) silicate hydrate chemistry under equilibrium conditions, Cem. Concr. Res. 68 (2015) 83–93.
[38] L. Greenspan, Humidity fixed points of binary saturated aqueous solutions, J. Res. Natl. Bur. Stand. 81 (1977) 89–96.
[39] Agilent Technologies, Nano Indenter G200 User's Guide Palo Alto, California, (2013).
[40] R. Saha, W.D. Nix, Effects of the substrate on the determination of thin film mechanical properties by nanoindentation, Acta Mater. 50 (2002) 23–38.
[41] G. Dushaq, A. Nayfeh, M. Rasras, Hexagonal germanium formation at room temperature using controlled penetration depth nano-indentation, Sci. Rep. 9 (2019)

1593.
[42] X. Li, B. Bhushan, A review of nanoindentation continuous stiffness measurement technique and its applications, Mater. Charact. 48 (2002) 11–36.
[43] S. Mantellato, M. Palacios, R.J. Flatt, Impact of sample preparation on the specific surface area of synthetic ettringite, Cem. Concr. Res. 86 (2016) 20–28.
[44] M.M. Costoya Fernández, Effect of Particle Size on the Hydration Kinetics and Microstructural Development of Tricalcium Silicate, EPFL, 2008 (Doctoral Dissertation).
[45] R.W. Heckel, Density-pressure relationships in powder compaction, Trans. Metall. Soc. AIME 221 (1961) 671–675.
[46] A.J. Allen, J.J. Thomas, H.M. Jennings, Composition and density of nanoscale calcium–silicate–hydrate in cement, Nat. Mater. 6 (2007) 311.
[47] H.M. Jennings, Refinements to colloid model of CSH in cement: CM-II, Cem. Concr. Res. 38 (2008) 275–289.
[48] J.F. Young, W. Hansen, Volume relationships for CSH formation based on hydration stoichiometries, MRS Online Proc. Libr. Arch. 85 (1986).
[49] C.Y. Wu, O.M. Ruddy, A.C. Bentham, B.C. Hancock, S.M. Best, J.A. Elliott, Modelling the mechanical behaviour of pharmaceutical powders during compaction, Powder Technol. 152 (2005) 107–117.
[50] H. Leuenberger, B.D. Rohera, Fundamentals of powder compression. I. The compactibility and compressibility of pharmaceutical powders, Pharm. Res. 3 (1986) 12–22.
[51] J.A. Hersey, J.E. Rees, Deformation of particles during briquetting, Nat. Phys. Sci. 230 (1971) 96.
[52] C. Sun, D.J.W. Grant, Influence of elastic deformation of particles on Heckel analysis, Pharm. Dev. Technol. 6 (2001) 193–200.
[53] E. L'Hôpital, B. Lothenbach, D.A. Kulik, K. Scrivener, Influence of calcium to silica ratio on aluminium uptake in calcium silicate hydrate, Cem. Concr. Res. 85 (2016) 111–121.
[54] H.M. Jennings, J.J. Thomas, J.S. Gevrenov, G. Constantinides, F.-J. Ulm, A multi-technique investigation of the nanoporosity of cement paste, Cem. Concr. Res. 37 (2007) 329–336.
[55] H.M. Jennings, A. Kumar, G. Sant, Quantitative discrimination of the nano-pore-structure of cement paste during drying: new insights from water sorption isotherms, Cem. Concr. Res. 76 (2015) 27–36.
[56] M. Wyrzykowski, P.J. McDonald, K.L. Scrivener, P. Lura, Water redistribution within the microstructure of cementitious materials due to temperature changes studied with 1H NMR, J. Phys. Chem. C 121 (2017) 27950–27962.
[57] K. Scrivener, R. Snellings, B. Lothenbach, A Practical Guide to Microstructural Analysis of Cementitious Materials, CRC Press, 2016.
[58] F.J. Trojer, The crystal structure of parawollastonite, Z. Krist. Cryst. Mater. 127 (1968) 291–308.
[59] S. Martinez-Ramirez, M. Frías, C. Domingo, Micro-Raman spectroscopy in white portland cement hydration: long-term study at room temperature, J. Raman Spectrosc. 37 (2006) 555–561.
[60] K. Garbev, P. Stemmermann, L. Black, C. Breen, J. Yarwood, B. Gasharova, Structural features of C–S–H (I) and its carbonation in air—a Raman spectroscopic study. Part I: fresh phases, J. Am. Ceram. Soc. 90 (2007) 900–907.
[61] M. Tarrida, M. Madon, B. Le Rolland, P. Colombet, An in-situ Raman spectroscopy study of the hydration of tricalcium silicate, Adv. Cem. Based Mater. 2 (1995) 15–20.
[62] S. Ortaboy, J. Li, G. Geng, R.J. Myers, P.J.M. Monteiro, R. Maboudian, C. Carraro, Effects of CO_2 and temperature on the structure and chemistry of C–(A–) S–H investigated by Raman spectroscopy, RSC Adv. 7 (2017) 48925–48933.
[63] R.J. Kirkpatrick, J.L. Yarger, P.F. McMillan, Y. Ping, X. Cong, Raman spectroscopy of CSH, tobermorite, and jennite, Adv. Cem. Based Mater. 5 (1997) 93–99.
[64] J. Li, G. Geng, R. Myers, Y.-S. Yu, D. Shapiro, C. Carraro, R. Maboudian, P.J.M. Monteiro, The chemistry and structure of calcium (alumino) silicate hydrate: a study by XANES, ptychographic imaging, and wide- and small-angle scattering, Cem. Concr. Res. 115 (2019) 367–378.
[65] S.W. Wang, L.D. Chen, T. Hirai, Densification of Al_2O_3 powder using spark plasma sintering, J. Mater. Res. 15 (2000) 982–987.
[66] G. Geng, R.J. Myers, M.J.A. Qomi, P.J.M. Monteiro, Densification of the interlayer spacing governs the nanomechanical properties of calcium-silicate-hydrate, Sci. Rep. 7 (2017) 10986.
[67] C.A. Ross, J.W. Tedesco, S.T. Kuennen, Effects of strain rate on concrete strength, Mater. J. 92 (1995) 37–47.
[68] D. Ménétrier, I. Jawed, T.S. Sun, J. Skalny, ESCA and SEM studies on early C3S hydration, Cem. Concr. Res. 9 (1979) 473–482.
[69] G. Kakali, S. Tsivilis, E. Aggeli, M. Bati, Hydration products of C3A, C3S and Portland cement in the presence of CaCO3, Cement and Concrete Research 30 (2000) 1073–1077.
[70] J.J. Beaudoin, Comparison of mechanical properties of compacted calcium hydroxide and Portland cement paste systems, Cem. Concr. Res. 13 (1983) 319–324.
[71] P. Acker, Micromechanical analysis of creep and shrinkage mechanisms, Creep, Shrinkage and Durability Mechanics of Concrete and Other Quasi-Brittle Materials, Cambridge, MA, 2001, pp. 15–25.
[72] F.J. Ulm, M. Vandamme, C. Bobko, J. Alberto Ortega, K. Tai, C. Ortiz, Statistical indentation techniques for hydrated nanocomposites: concrete, bone, and shale, J. Am. Ceram. Soc. 90 (2007) 2677–2692.
[73] J.J. Hughes, P. Trtik, Micro-mechanical properties of cement paste measured by depth-sensing nanoindentation: a preliminary correlation of physical properties with phase type, Mater. Charact. 53 (2004) 223–231.
[74] F. Linde, P. Nørgaard, I. Hvid, A. Odgaard, K. Søballe, Mechanical properties of trabecular bone. Dependency on strain rate, J. Biomech. 24 (1991) 803–809.
[75] X.Q. Shi, W. Zhou, H.L.J. Pang, Z.P. Wang, Y.P. Wang, Effect of temperature and strain rate on mechanical properties of 63Sn/37Pb solder alloy, Am. Soc. Mech. Eng. J. Electron. Packag. 121 (1999) 179–185.
[76] G.C. Jacob, J.M. Starbuck, J.F. Fellers, S. Simunovic, R.G. Boeman, Strain rate effects on the mechanical properties of polymer composite materials, J. Appl. Polym. Sci. 94 (2004) 296–301.
[77] K.S.W. Sing, Reporting physisorption data for gas/solid systems with special reference to the determination of surface area and porosity (Recommendations 1984), Pure Appl. Chem. 57 (1985) 603–619.
[78] O.A. Odeku, The compaction of pharmaceutical powders, Pharm. Inf. Artic. Latest Rev. (2007) 5.
[79] A. Michrafy, J.A. Dodds, M.S. Kadiri, Wall friction in the compaction of pharmaceutical powders: measurement and effect on the density distribution, Powder Technol. 148 (2004) 53–55.
[80] I.C. Sinka, J.C. Cunningham, A. Zavaliangos, The effect of wall friction in the compaction of pharmaceutical tablets with curved faces: a validation study of the Drucker–Prager Cap model, Powder Technol. 133 (2003) 33–43.
[81] P. Mehta, P.J.M. Monteiro, Concrete: Microstructure, Properties, and Materials, 3rd ed., McGraw-Hill Professional, 2006.
[82] C.A. Jones, Z.C. Grasley, J.A. Ohlhausen, Measurement of elastic properties of calcium silicate hydrate with atomic force microscopy, Cem. Concr. Compos. 34 (2012) 468–477.
[83] W. Wilson, N.A. Soliman, L. Sorelli, A. Tagnit-Hamou, Micro-chemo-mechanical features of ultra-high performance glass concrete (UHPGC), Theor. Appl. Fract. Mech. 104 (2019) 102373.